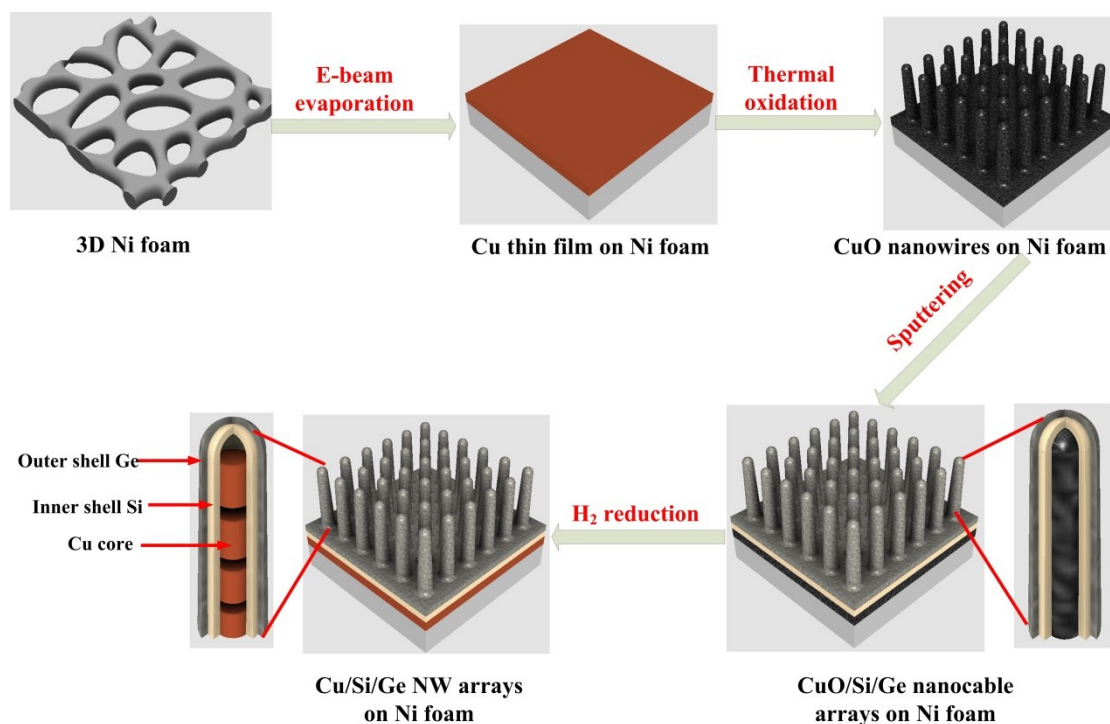
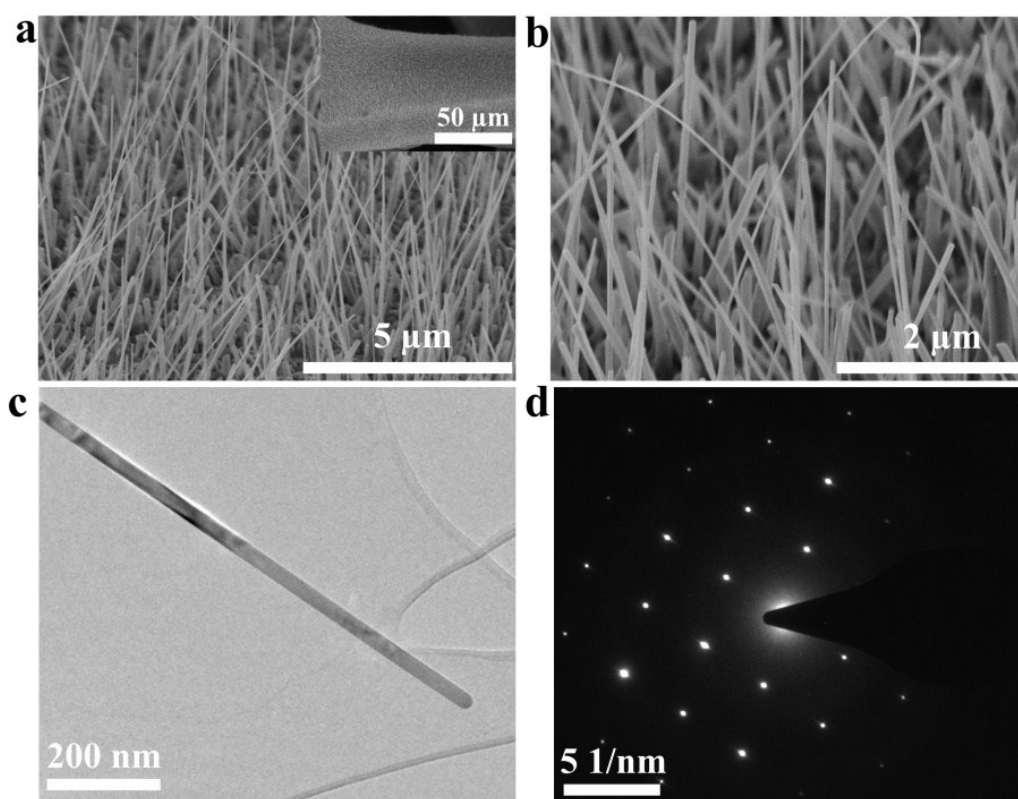


Supporting Information

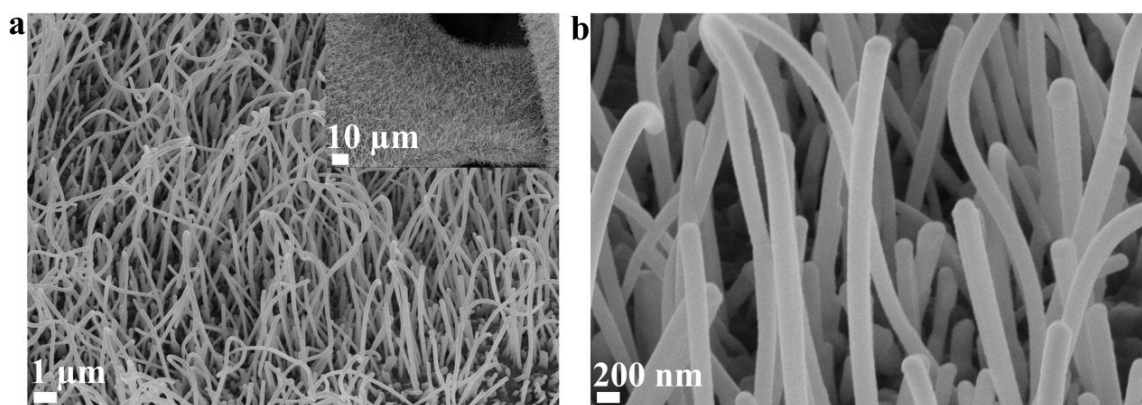
Harnessing the concurrent reaction dynamics in active Si and Ge to achieve high performance of lithium-ion batteries



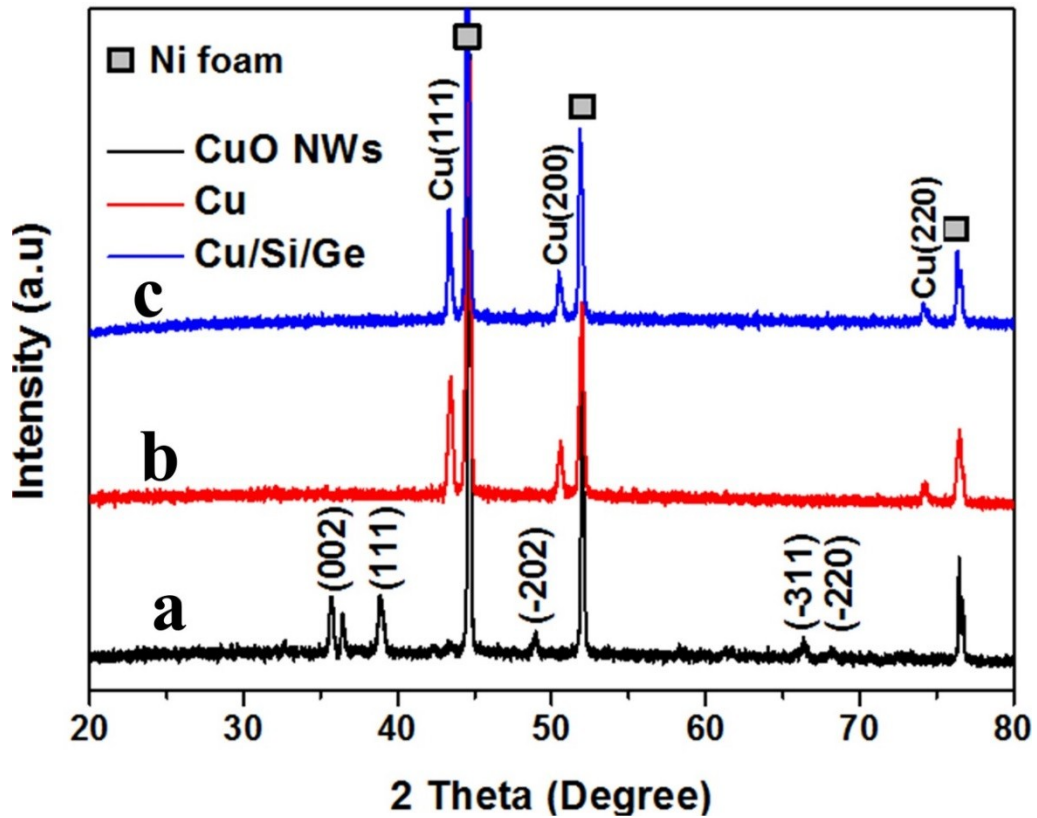
Supplementary Figure 1. Schematic of fabrication of the electrode consisting of Cu/Si/Ge NW arrays on a 3D porous Ni foam.



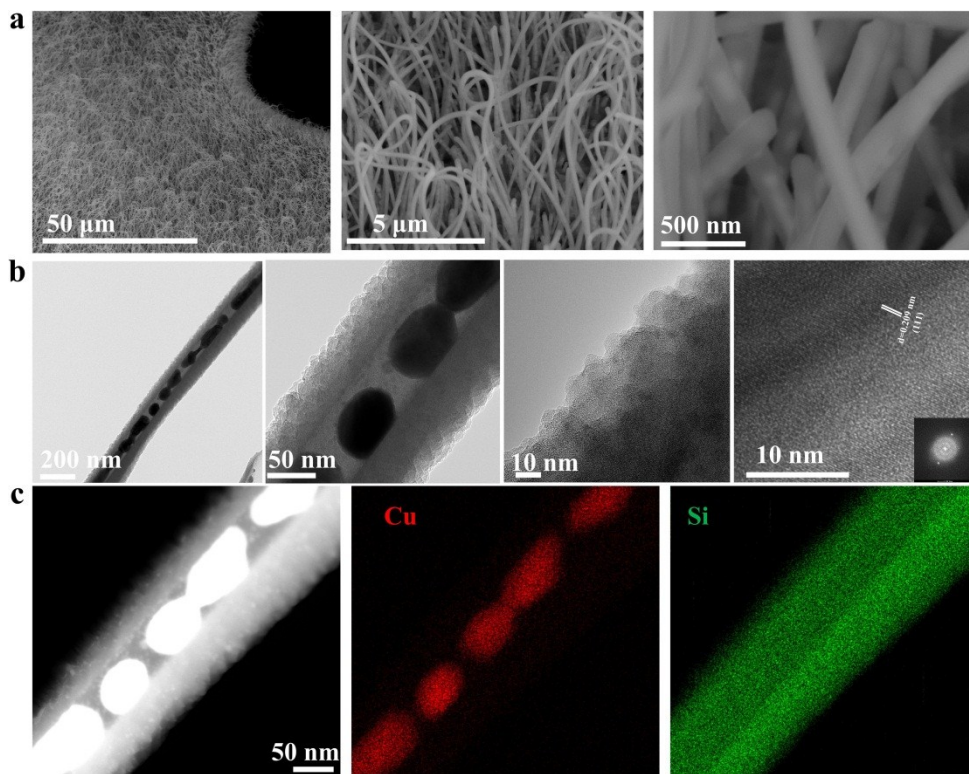
Supplementary Figure 2. Characterization of CuO nanowires grown on the surface of a Ni foam. **a, b**, SEM images of as-fabricated CuO nanowire arrays, with the corresponding low-magnification image in the inset of **a**. **c**, TEM image of individual CuO nanowire. **d**, Corresponding SAED pattern.



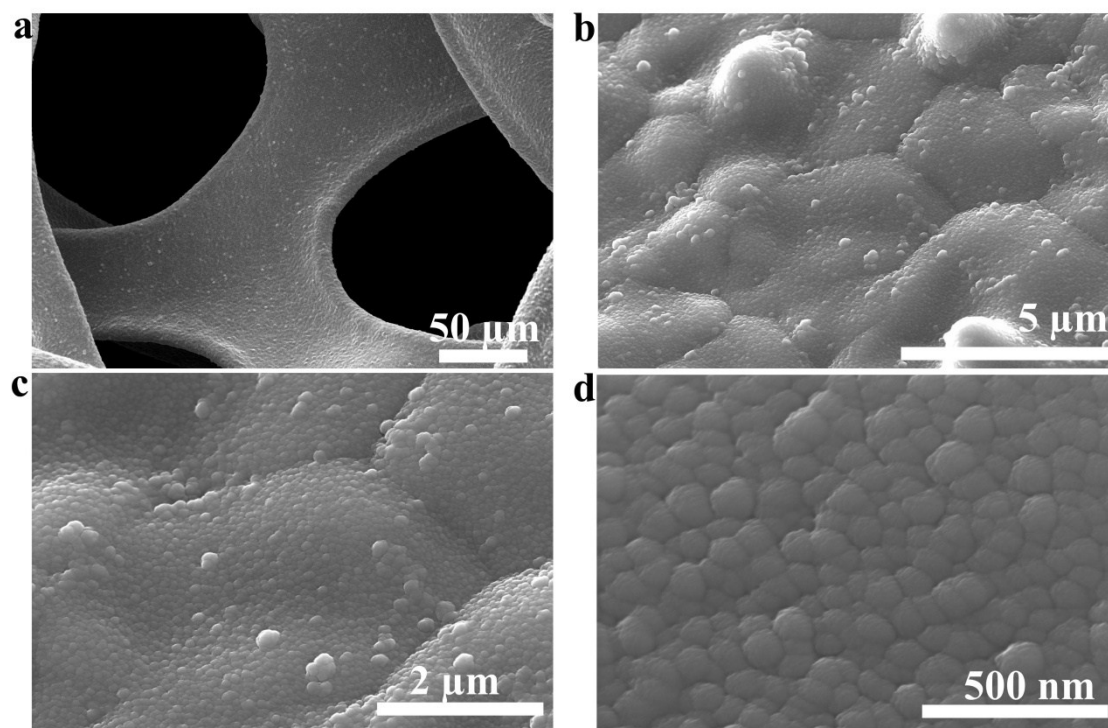
Supplementary Figure 3. Characterization of CuO/Si/Ge nanowire arrays grown on a Ni foam. **a, b**, SEM images of CuO/Si/Ge nanowire arrays, with the corresponding low-magnification image in the inset of **a**.



Supplementary Figure 4. XRD pattern of **a**, CuO nanowire arrays on a Ni foam; **b**, CuO nanowire arrays on a Ni foam after annealing at 300 °C in H₂/Ar (95% Ar and 5% H₂) for 8h and **c**, as-fabricated CuO/Si/Ge nanocable arrays on a Ni foam after annealing at 300 °C in H₂/Ar (95% Ar and 5% H₂).



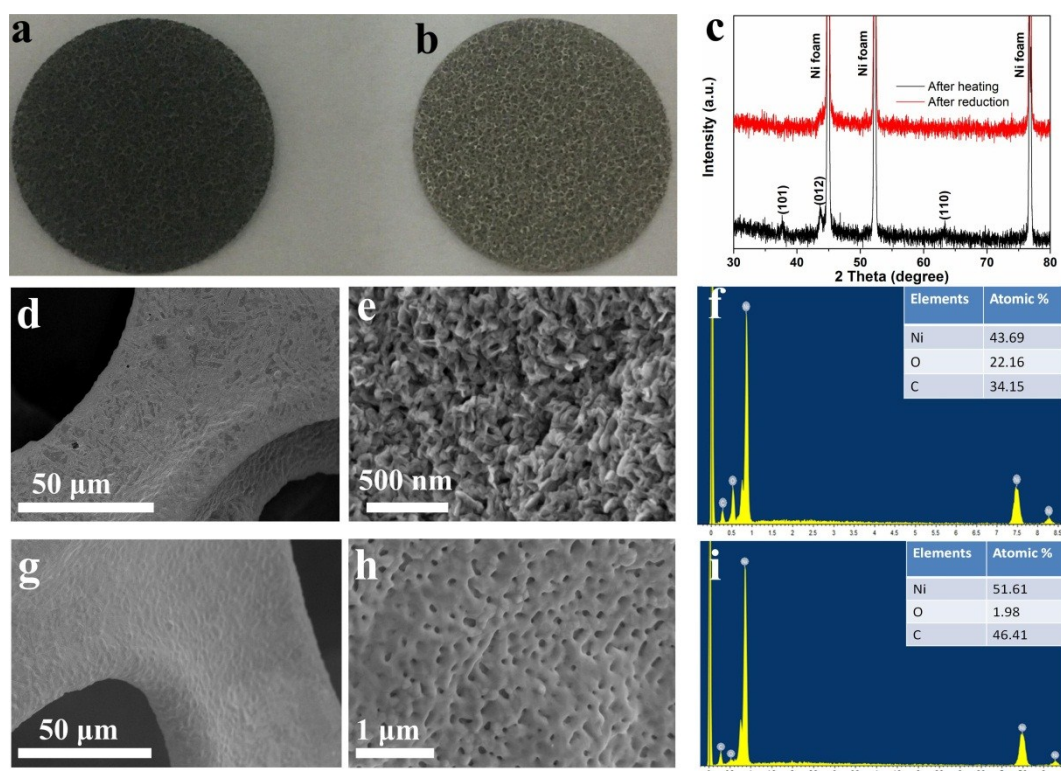
Supplementary Figure 5. a, SEM images of as-fabricated Cu/Si nanowire arrays on a Ni foam. b, TEM of single Cu/Si nanowire and c, its STEM image and corresponding Cu and Si X-ray maps.



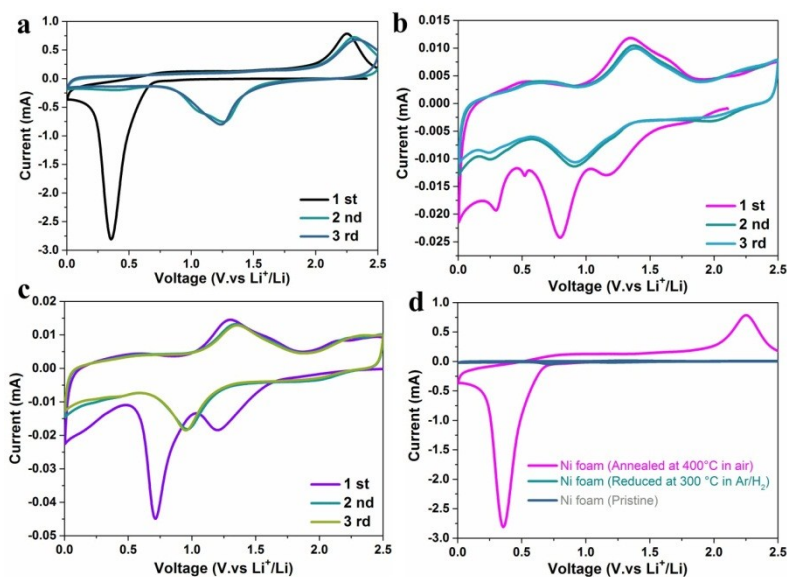
Supplementary Figure 6. SEM images of as-fabricated Si/Ge thin film on a Ni foam.

To check the possibility of capacity contribution from the Ni foam current collector, the electrochemical performance, microstructure and morphology of as-heated Ni foam (heating at 400°C for 12h in air), as-received and as-heated Ni foam after H₂/Ar at 300°C for 8h are compared. Indeed, heating of the Ni foam at 400°C for 12h in air can lead to a widespread formation of NiO nanoparticles on the surface as confirmed by characterization via SEM (Supplementary Figure 7d-e), XRD (Supplementary Figure 7b) and EDX (Supplementary Figure 7f) as well as by the color change of Ni foam to dark blue (Figure 7a), consistent with the reported results [1-3]. However, when the NiO/Ni foam substrates were annealed in H₂/Ar at 300°C for 8h, it can be seen that the NiO on the surface of the Ni foam can be successfully reduced as confirmed by characterization via SEM (Supplementary Figure 7g-h), XRD (Supplementary Figure 7b) and EDX (Supplementary Figure 7i) as well as by the color change from dark blue to the original color of Ni foam (Supplementary Figure 7b). To check the electrochemical responses of as-received Ni foam substrates, a heat treated Ni foam substrate and a heat treated Ni foam substrate after annealing in H₂/Ar, we compared the cyclic voltammogram measurements at a scan rate of 0.2 mVs⁻¹ over the potential window of 0.005–2.5 V versus Li/Li⁺ for those samples, as shown in Supplementary Figure 8. As seen in Supplementary Figure 8a, the Ni foam sample heated to 400°C had a strong cathodic peak at 0.36 V in the first scan, corresponds to the initial reduction of NiO to metallic Ni and the formation of amorphous Li₂O and the SEI layer. Two peaks in the initial anodic scan at 1.72 and 2.24 V are associated with the formation of NiO and the decomposition of Li₂O and the

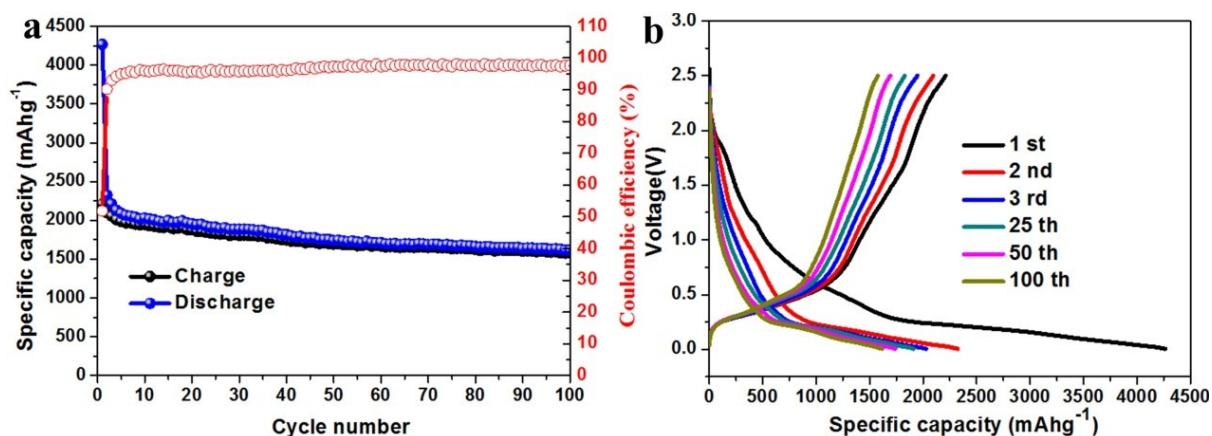
SEI layer.^[1, 3] This result indicates the Ni foam subjected to high temperature annealing shows substantial electrochemical contributions which may lead to inflated capacities and incorrect interpretation of CV responses for samples. The CV scans for the Ni foam sample heated to 400°C are in close agreement with previous reports on various NiO nanostructures [4-6], indicating that there is a significant amount of NiO present on the surface of the foam after heating. This is also in close agreement with the XRD, SEM and EDX results shown in Supplementary Figure 7. However, after the NiO/Ni foam substrates were annealed in H₂/Ar at 300°C for 8h (Figure 8b), the cathodic peak currents at 0.38 V (which originated from the NiO [1]) and 0.72V [1] (which was associated with the native NiO layer on Ni foam as well as the CV integrated area) decrease significantly, suggesting the NiO on the surface of Ni foam can be reduced extensively and the NiO/Ni foam substrates after annealed in H₂/Ar show negligible electrochemical activity. The first CV scan for each sample is overlaid in Supplementary Figure 8d. It is clear that the measured current values of the initial cathodic peak for the as received Ni foam and the heat treated Ni foam after annealed in H₂/Ar are quite low (<-0.05 mA) in comparison with that of heat treated Ni foam. All these results indicate that the capacity of the heat treated Ni foam after annealed in H₂/Ar at 300°C for 8h are negligible.



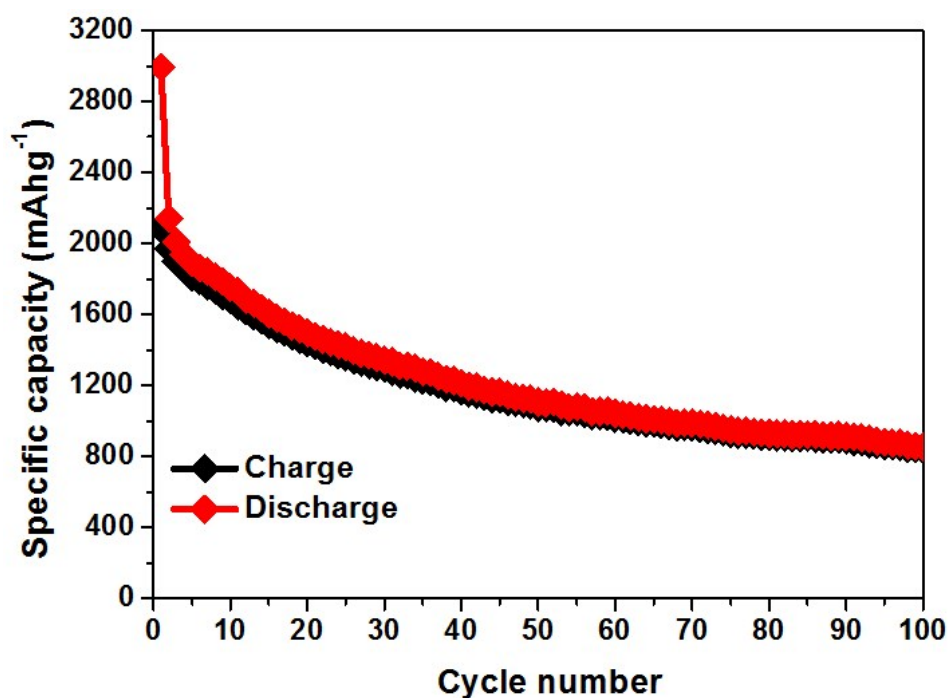
Supplementary Figure 7. a, Photograph of a Ni foam after annealing at 400°C for 12h in air. b, Photograph of an as-heated Ni foam after reduction at 300°C for 8h in Ar/H₂. c, XRD patterns of Ni foam after annealing at 400°C for 12h in air (black line) and after reduction at 300°C for 8h in Ar/H₂ (red line). d-e, SEM images of Ni foam after annealing at 400°C for 12h in air and f, corresponding EDX spectra. g-h, SEM images of as-heated Ni foam after reduction at 300°C for 8h in Ar/H₂ and i, corresponding EDX spectra.



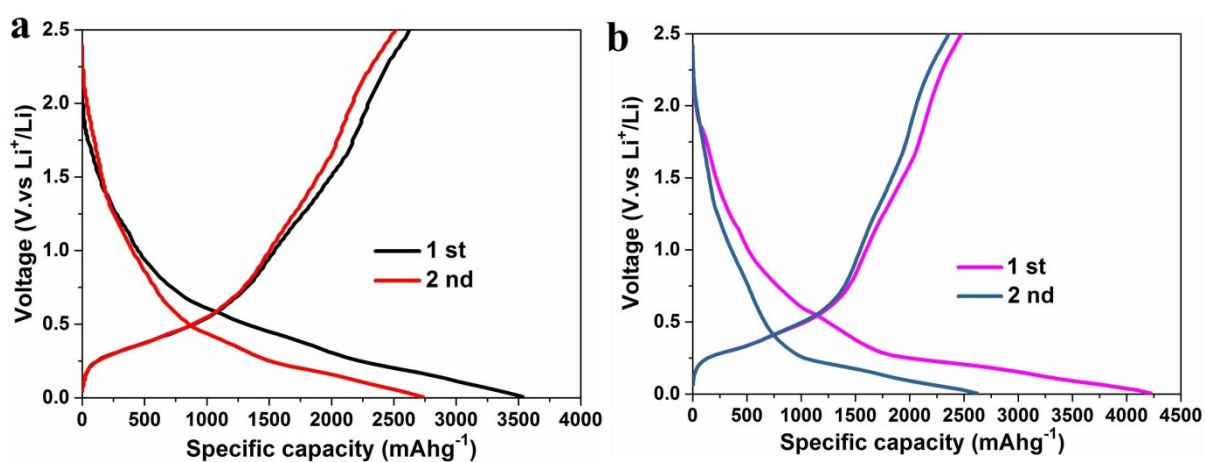
Supplementary Figure 8. Cyclic voltammograms at a scan rate of 0.2 mV s^{-1} in the voltage window of 0.005–2.5 V versus Li/Li^+ for **a**, Ni foam heated at 400°C for 12h in air; **b**, as-heated Ni foam after reduction at 300°C for 8h in Ar/H_2 ; **c**, as-received bare Ni foam. **d**, Comparison of the first CV scan for as-received bare Ni foam, Ni foam heated at 400°C for 12h in air, and the as-heated Ni foam after reduction at 300°C for 8h in Ar/H_2 at a scan rate of 0.2 mV s^{-1} .



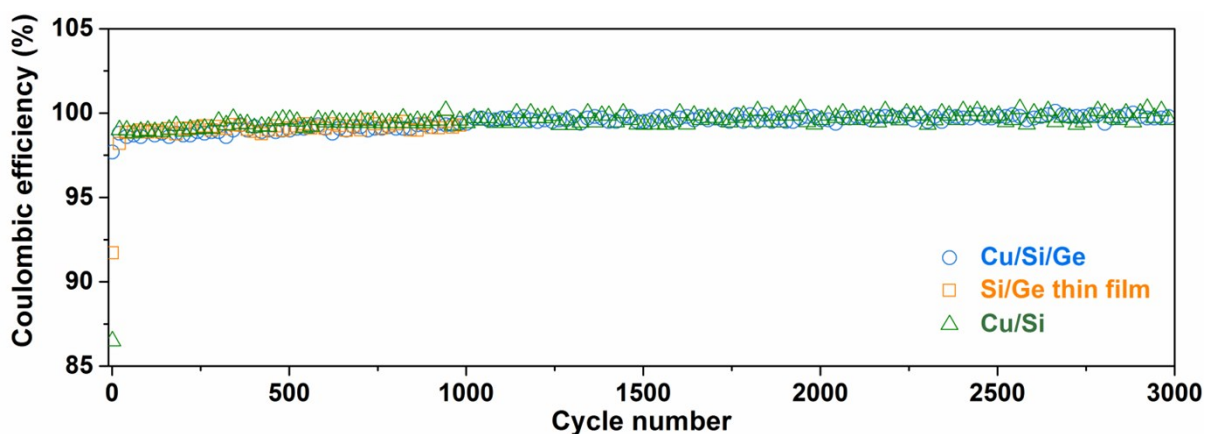
Supplementary Figure 9. Electrochemical data of the Cu/Si NW electrode. **a**, Cycling performance of Cu/Si NW arrays electrode at 0.4 Ag^{-1} (0.2 C) for 100 cycles. **b**, Corresponding galvanostatic charge–discharge profiles for the first, second, third, 25th, 50th and 100th cycle.



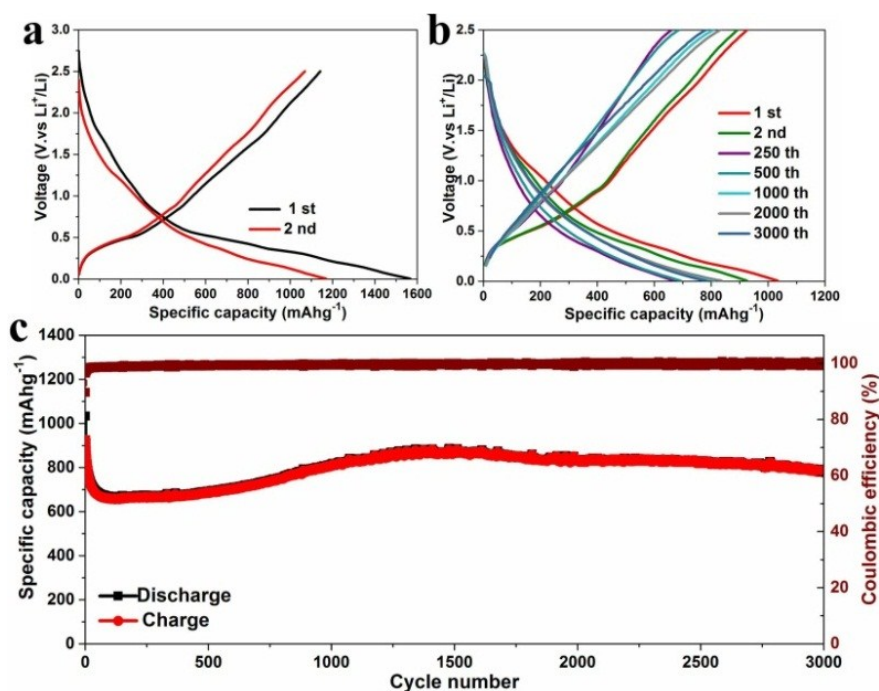
Supplementary Figure 10. Cycling performance of the Si/Ge thin-film electrode at a current density 0.4 Ag⁻¹.



Supplementary Figure 11. Galvanostatic charge–discharge profiles for the first and second cycle of a, Cu/Si/Ge NW electrode and b, Cu/Si NW electrode at 0.2C.



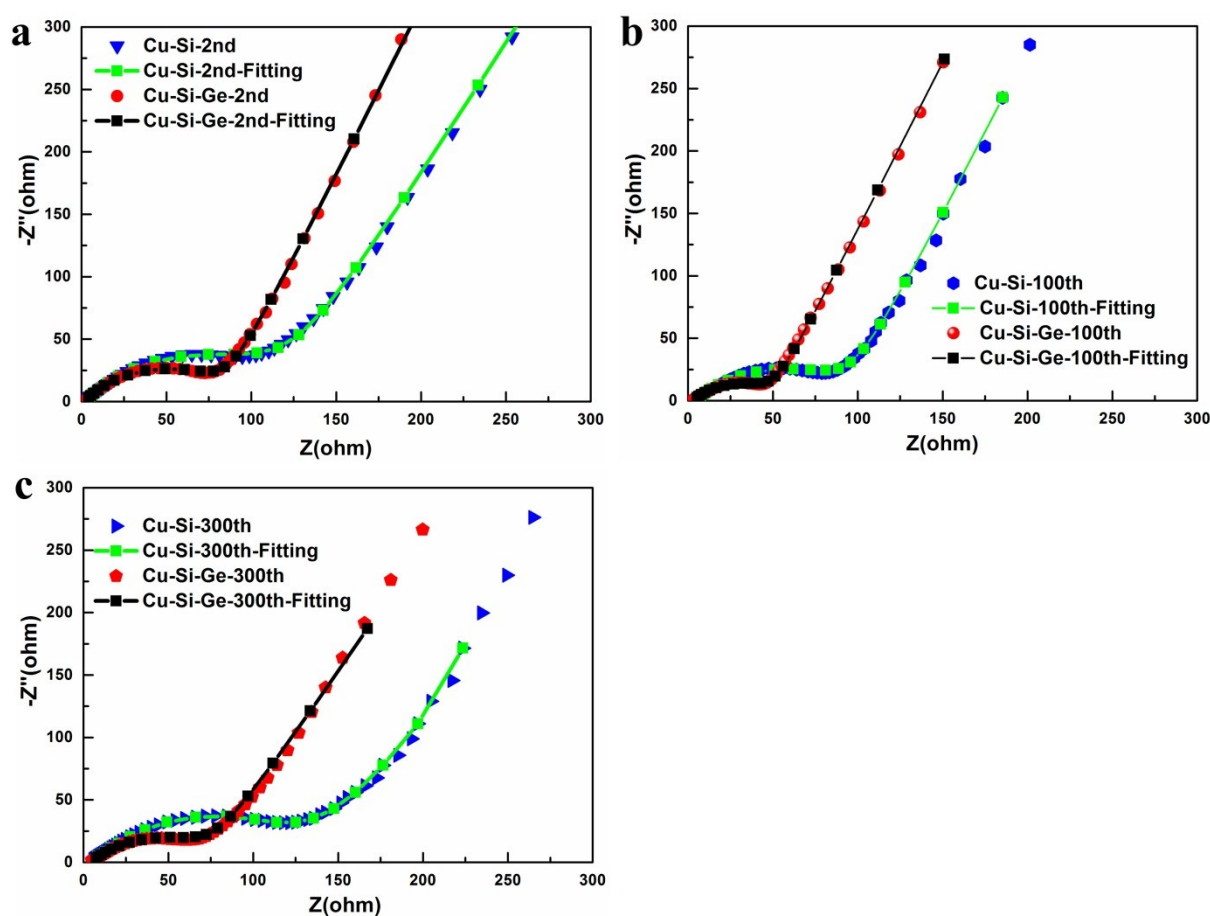
Supplementary Figure 12. Coulombic efficiencies of different electrodes made of Cu/Si/Ge NWs, Si/Ge thin films and Cu/Si NWs at a rate of 2C.



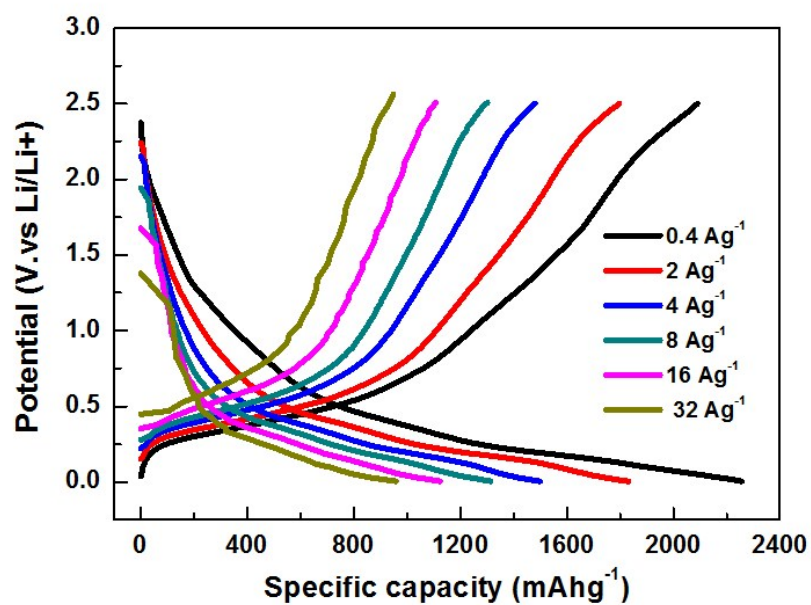
Supplementary Figure 13. a, Galvanostatic charge–discharge profiles of Cu/Ge at 0.2C for two cycles. b, Galvanostatic charge–discharge profiles at 2C for different cycles. c, Corresponding cycling performance at 2C for 3000 cycles. The electrode was first activated at a low rate of 0.2C for two cycles as shown in Supplementary Figure 11a and then subjected to 2C for long-term cycling.

Supplementary Figure 14 shows the electrochemical impedance spectroscopy (EIS) data for both Cu/Si/Ge and Cu/Si electrodes over the frequency range from 1 MHz to 10 mHz with an AC amplitude of 5 mV. The spectra are composed of one semicircle in the high frequency region (arising from impedance to the charge transfer process, and an inclined line in the low frequency region (arising from impedance to the diffusion of lithium ions). The charge transfer

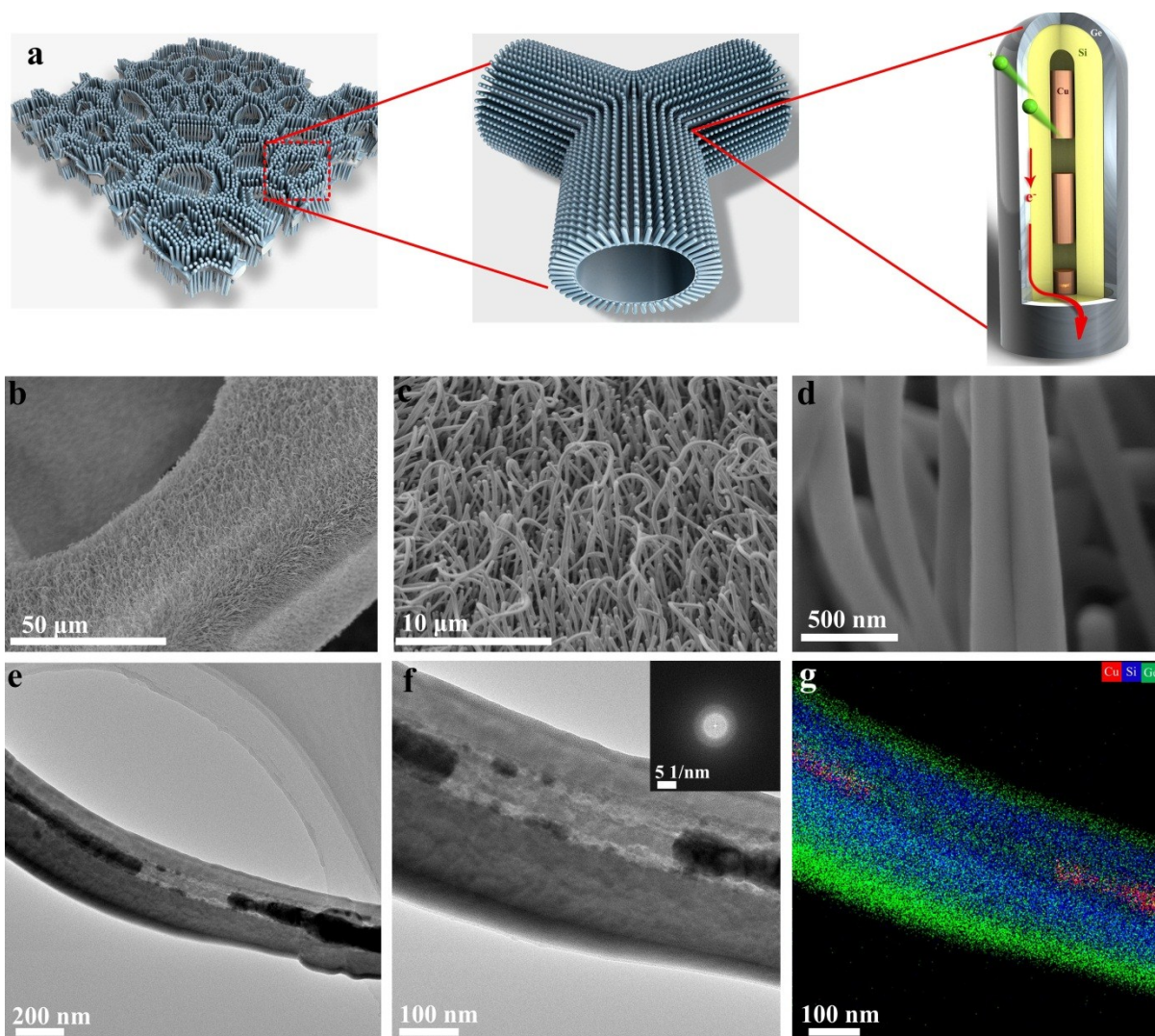
resistances after the 2nd (Figure 14a), 100th (Figure 14b), 300th cycle (Figure 14c) are determined to be about 60 Ω , 39 Ω and 61 Ω for the Cu/Si/Ge electrode and 70 Ω , 83 Ω and 114 Ω for the Cu/Si electrode, respectively. Hence, the Cu/Si/Ge electrode shows much lower charge-transfer impedance than the Cu/Si electrode, an indication of the faster charge transfer and higher electrode conductivity. As a result, Li ion diffusion and electron transfer are expedited at high cycling rates for the Cu/Si/Ge electrode. Moreover, the charge transfer resistances of the Cu/Si electrode exhibited a continuous and marked increase upon cycling, resulting in a 1.6-fold increase after 300 cycles. In contrast, the charge transfer resistances of the Cu/Si/Ge increased slightly from 60 to 61 Ω upon cycling. This indicates that the presence of the Ge outer layer facilitates the improvement of cycling stability. These results indicate the Ge outer layer plays a key role in the performance enhancement of the Si-based electrode.



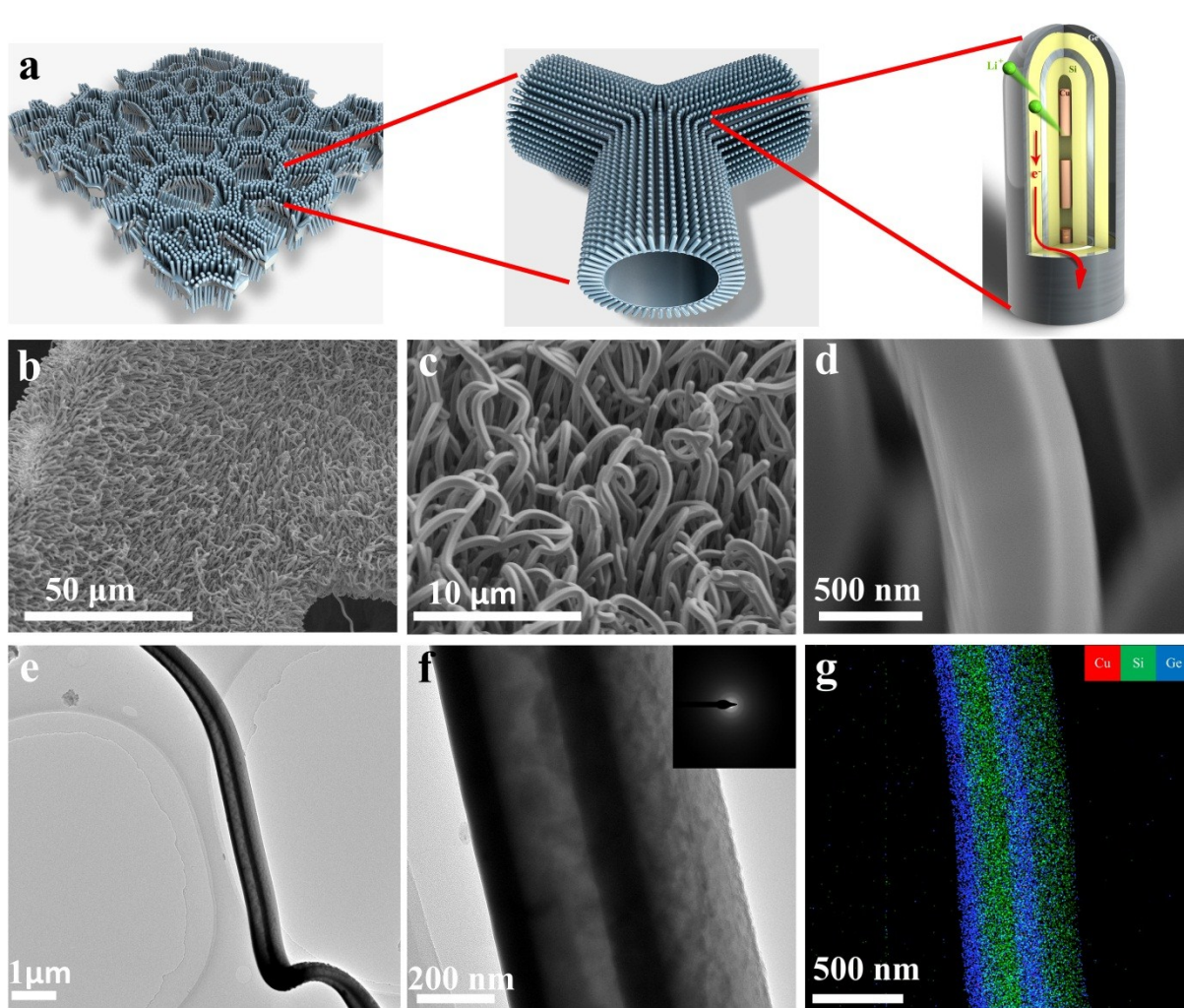
Supplementary Figure 14. Electrochemical impedance spectroscopy EIS results of the Cu/Si/Ge electrode under a, the second cycle. b, 100 cycle and c, 300 cycle at 4Ag^{-1} .



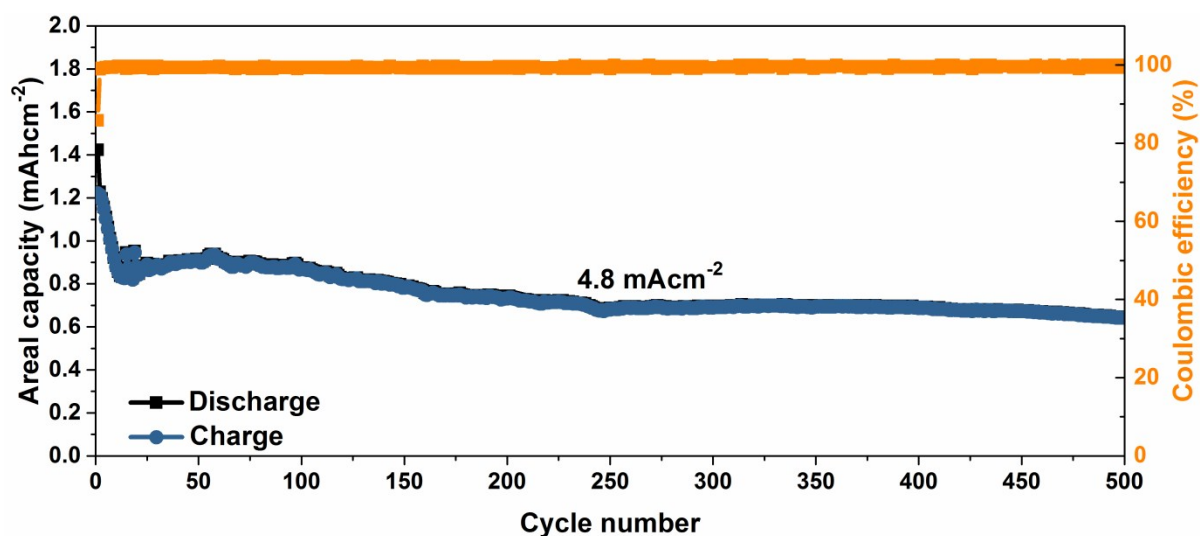
Supplementary Figure 15. Galvanostatic charge–discharge profiles of the Cu/Si/Ge nanotube arrays electrode at various current densities ranging from 0.4 Ag⁻¹ from 32 Ag⁻¹.



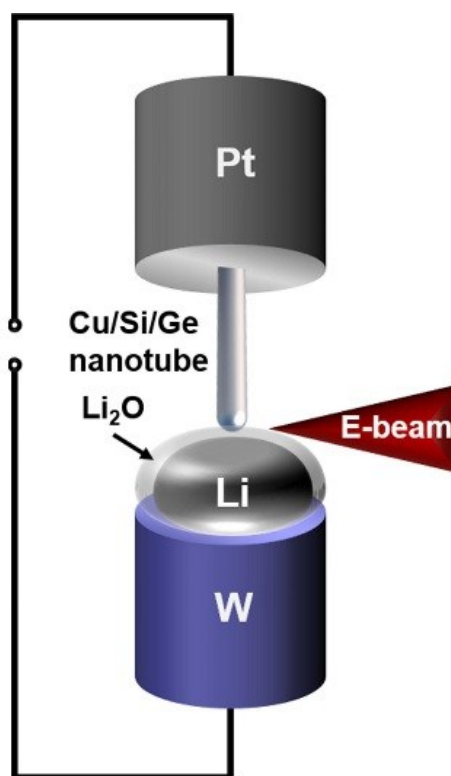
Supplementary Figure 16. a, Schematic illustration of electrode structure consisting of Cu/Si/Ge NW arrays with doubled thickness of both Si and Ge layers; NW arrays are grown on both front and back faces of a 3D porous Ni foam. b-d, SEM images and e-f, TEM images of Cu/Si/Ge NW arrays with doubled thickness of both Si and Ge layers. g, STEM image and corresponding Cu, Si and Ge EDX maps.



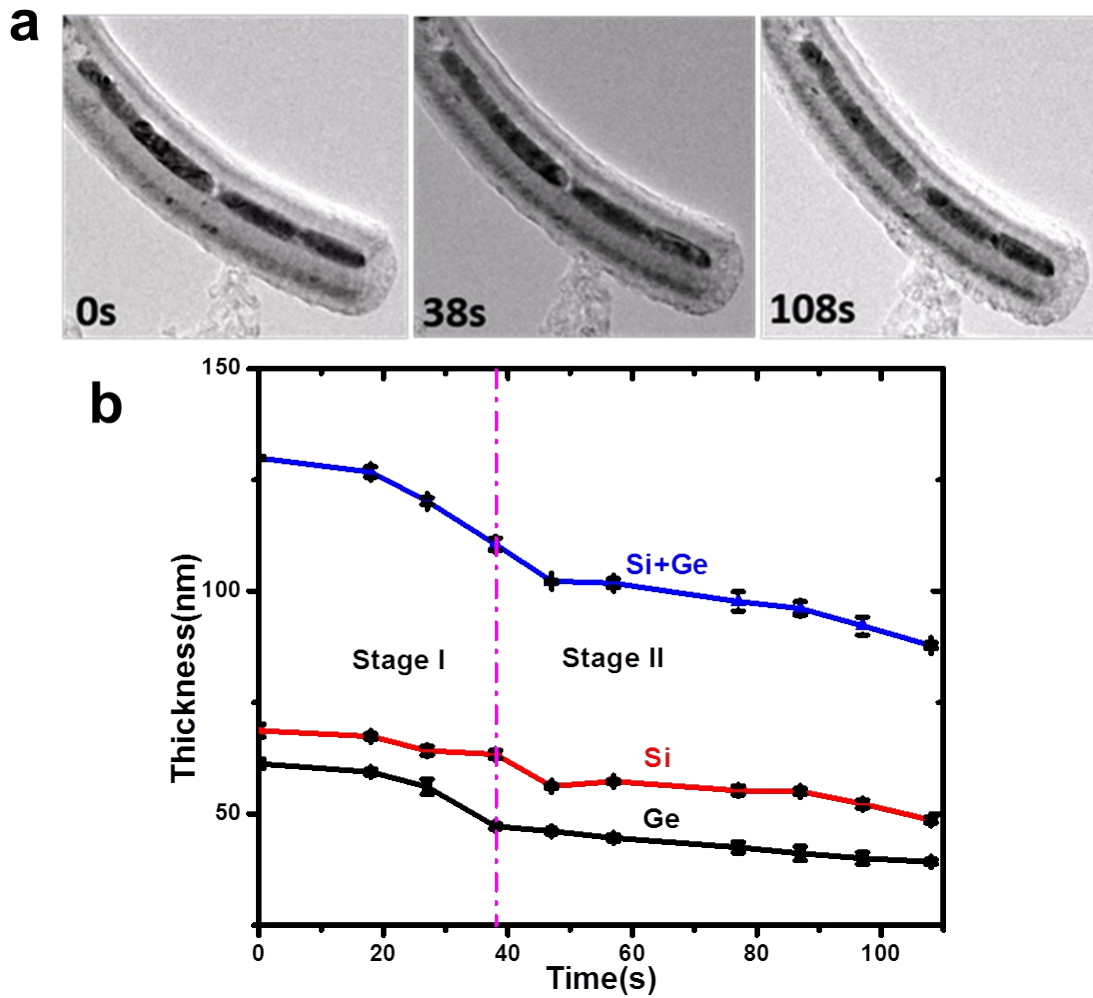
Supplementary Figure 17. a, Schematic illustration of the electrode structure consisting of Cu/Si/Ge/Si/Ge NW arrays with double layers of the Si/Ge bilayer shell; the NW array was grown on both front and back faces of a 3D porous Ni foam. b-d, SEM images and e-f, TEM images of Cu/Si/Ge NW arrays with doubled thickness of both Si and Ge layers. g, STEM image and corresponding Cu, Si and Ge EDX maps.



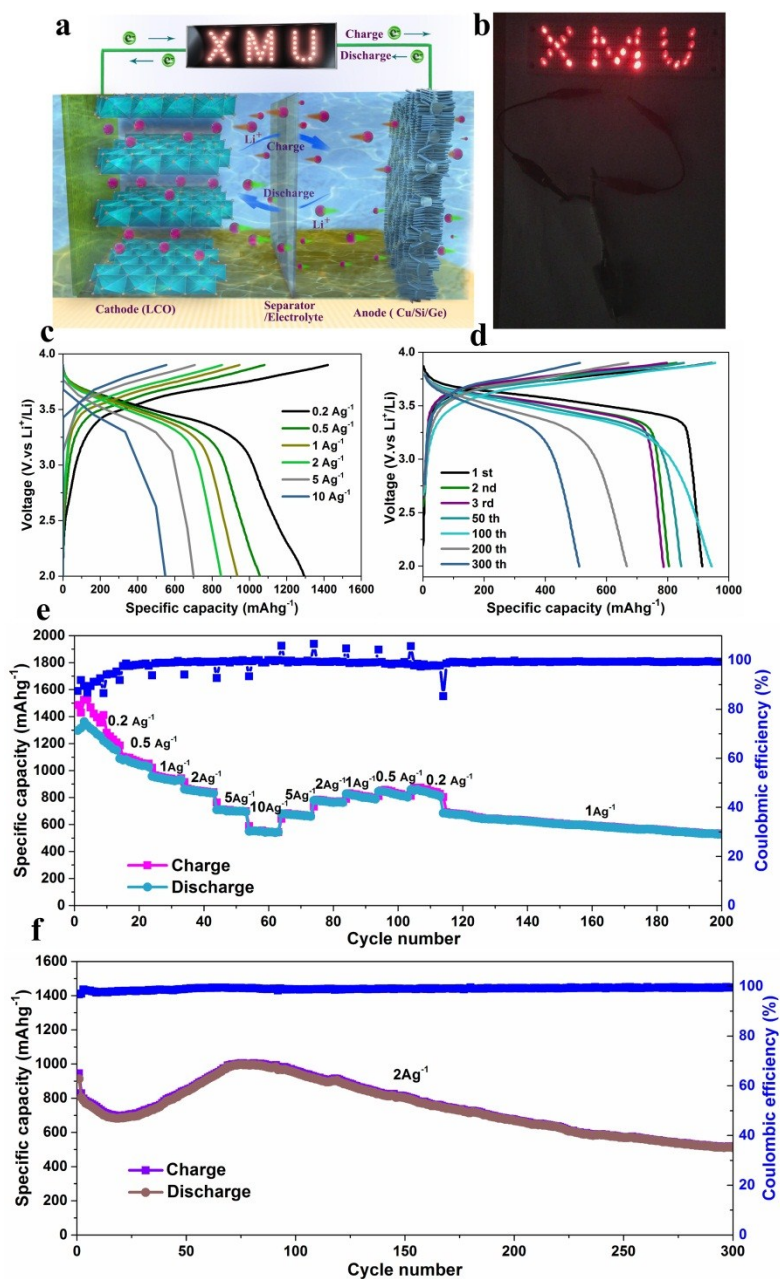
Supplementary Figure 18. Electrochemical performance of the Cu/Si/Ge NW electrode with a mass loading of 1.2 mgcm^{-2} . Long-cycle performance at an areal current density of 4.8 mAcm^{-2} (4 Ag^{-1}) for 500 cycles; the electrodes were first activated at 0.48 mAcm^{-2} for two cycles and then subjected to long-term cycling at 4.8 mAcm^{-2} .



Supplementary Figure 19. Schematic of the *in situ* TEM nano-battery testing setup.



Supplementary Figure 20. *In situ* TEM results of delithiation of a single Cu/Si/Ge NW. a, Time-lapse TEM snapshots during delithiation. b, Measured thicknesses of Si, Ge and Si/Ge layers as a function of time during delithiation.



Supplementary Figure 21. Electrochemical data of a full cell with the Cu/Si/Ge NW anode under a high mass loading of about 0.6 mgcm^{-2} . a, Schematic illustration of the full cell. b, Operation of a full cell lighting up an LED array with a XMU (Xiamen University) logo. c, Charge-discharge curves at various rates. d, Charge-discharge curves at a current density of 2 Ag^{-1} . e, Rate performance at various rates and f, Cycling performance at a current density of 2 Ag^{-1} .

Supplementary Table 1. A summary of the performances of different Si-based core/shell nanowire or nanotube structures and Si/Ge core/shell or nanotube structures from the 2nd to the last cycle in the literature,^[7-25] in comparison with the results in this work.

Materials and structures	Thickness of Si or Si/Ge (nm)	Current density (Ag^{-1})	Cycles	Capacity after cycles (mAhg^{-1})	Areal Capacity after cycles (mAh cm^{-2})	Capacity retention (%)	References
C@Si@C Nanotube array	≈ 20	0.3 0.2-8.4	60 40	≈ 2200 ≈ 1240	unavailable	≈ 69 ≈ 50	[7]
Cu-Si core shell Nanotube arrays	≈ 50 (0.3mgcm^{-2})	0.84 1.3-34	400 35	≈ 1500 ≈ 633	≈ 0.45 ≈ 0.19	≈ 60 ≈ 30	[8]
CNT-Si Composite	≈ 100 (0.12mgcm^{-2})	2.0 2.0-3.0	50 30	≈ 980 ≈ 1042	≈ 0.12 ≈ 0.13	≈ 57 ≈ 76	[9]
Cu-Li ₂ O@a-Si Core shell array	≈ 40 (0.025mgcm^{-2})	0.84 0.2-4.2	100 25	≈ 2200 ≈ 520	≈ 0.055 ≈ 0.013	≈ 94 ≈ 18	[10]
Si nanotube	≈ 30 ($0.02-0.1\text{mgcm}^{-2}$)	0.4 2.0-24	900 280	≈ 1353 ≈ 940	$\approx 0.03-0.14$ $\approx 0.02-0.09$	≈ 76 ≈ 52	[11]
Cu-Si-Al ₂ O ₃ Nanocable array	≈ 100	1.4 0.3-14	100 45	≈ 1560 ≈ 790	unavailable	≈ 90 ≈ 43	[12]
CNT-Si core shell NW	≈ 55 (2mgcm^{-2})	0.84 0.84-34	80 60	≈ 2510 ≈ 1170	≈ 5.02 ≈ 2.34	≈ 91 ≈ 44	[13]
Cu-Si _{1-x} Ge _x Core shell NW array	≈ 60	4.0 2-32	75 30	≈ 1500 ≈ 1348	unavailable	≈ 75 ≈ 67	[14]
Coaxial Cu-Si@C array	≈ 45	0.8 0.8-8.0	50	≈ 2400 ≈ 1050	unavailable	≈ 82 44	[15]
C-Si@a-Si core shell NW array	≈ 47 (0.2mgcm^{-2})	3.4	100	≈ 880	≈ 0.18	99	[16]
CNT-Ni-Si NW array	≈ 50 (0.08mgcm^{-2})	0.84 0.84-33	110 60	≈ 1986 ≈ 1046	≈ 0.16 ≈ 0.08	≈ 78 ≈ 42	[17]
a-Si/carbon Nanofiber NW array	≈ 60 (1.2mgcm^{-2})	0.5 0.5-2.5	55 70	≈ 1600 ≈ 800	≈ 1.92 ≈ 0.96	≈ 84 ≈ 61	[18]
Connected Cu-Si alloy nanotube	≈ 120 (0.18mgcm^{-2})	3.4 1.8-18	1000 135	≈ 1000 ≈ 360	≈ 0.18 ≈ 0.06	≈ 84 ≈ 20	[19]
Si-Ge NT array	≈ 30 (0.68mgcm^{-2})	0.24 0.24-3.6	50 15	≈ 1312 ≈ 942	≈ 0.89 ≈ 0.64	≈ 85 ≈ 61	[20]
Si-Ge core shell NW array	≈ 40	0.24 0.24-3.6	50 25	≈ 1032 ≈ 1283	unavailable	≈ 72 ≈ 90	[21]
Si-Ge/Si core shell NW	≈ 40 (1mgcm^{-2})	0.24 12	400 200	≈ 1031 ≈ 515	≈ 1.03 ≈ 0.52	≈ 89 ≈ 82.4	[22]
Ge/Si core shell	≈ 60	0.24	100	≈ 1614	≈ 0.50	≈ 91	[23]

NW	(0.31mgcm ⁻²)	0.12-12	35	≈802	≈0.24	≈62	
Cu nanopillar/a-Si	≈130 (0.01mgcm ⁻²)	1	100	≈1627	≈0.02	≈83	[24]
		1-20	50	≈1000	≈0.01	≈40	
		1-40-40	300	≈996	≈0.01	≈40	
Cu/Si/Ge NW array	≈90 (0.15-0.18mgcm⁻²)	4	3000	1523	≈0.23-0.27	≈81	This work
		2-32	50	1010	≈0.15-0.18	≈60	
		2-32-2	1000	1728	≈0.26-0.31	≈87	
Cu/Si/Ge NW array	≈328 (1.2mgcm⁻²)	0.4	100	1052	≈1.26	≈62	This work
		4	500	537	≈0.64	≈52	
		1-16	50	447	≈0.54	≈31	

Captions of Supplementary Movies

Movie S1: *In situ* TEM observation of lithiation of a Cu/Si/Ge nanowire (the display was sped up by 8 times the real time of lithiation).

Movie S2: *In situ* TEM observation of delithiation of a lithiated Cu/Si/Ge nanowire (the display was sped up by 8 times the real time of delithiation).

Movie S3: *In situ* TEM observation of lithiation of a Cu/Si/Ge nanowire when an abrupt change of contact occurred between the nanowire and Li₂O/Li (the display was sped up by 8 times the real time of delithiation).

Movie S4: *In situ* TEM observation of lithiation of a Cu/Si/Ge nanowire (the front one) from which the lithiation kinetics data were extracted (Fig. 4c). The display was sped up by 16 times the real time of lithiation.

Chemomechanical modeling. We adopted an earlier model of two-phase lithiation of *a*-Si^[25] for simulations of lithiation in the Si/Ge nanotube (NT). Specifically, *a*-Si is assumed to be an isotropic elastic material, with Young's modulus and yield stress depending linearly on Li concentration. That is, Young's modulus and yield stress for Li_xSi are respectively $E = (100-60c)$ GPa and $\sigma_y = (5-4c)$ GPa, where c is the normalized Li concentration. Moreover, the anisotropic lithiation expansion coefficient β_{ij} for lithiated Si are taken as $\beta_r=1.15$, $\beta_\theta=0.17$ and $\beta_z=0.07$, based on our previous study for *a*-Si NT^[25]. On the other hand, Ge is also modeled as an isotropic elastic material with the linear dependence of both Young's modulus and yield

stress on Li concentration. That is, for Li_xGe , $E = (103-74c)$ GPa and $\sigma_y = (5-4c)$ GPa. To simulate stage I of lithiation of Ge only, the Li diffusivity in Ge is 1000 times higher than that in Si. Different from Li_xSi with anisotropic β_{ij} , the lithiation expansion coefficient of Li_xGe is assumed to be isotropic, i.e., $\beta_{ij} = \beta_0\delta_{ij}$, where δ_{ij} is the second order identity tensor. We assign $\beta_0 = 0.445$, which accounts for $\sim 280\%$ volume expansion of Ge after full lithiation. The boundary condition is imposed on the outer surface of the Si/Ge NT with the normalized Li concentration $c = 1$. The simulations are performed using the finite element package ABAQUS as described in our previous paper^[25].

References

- [1] H. Geaney, D. McNulty, J. O'Connell, J. D. Holmes, C. O'Dwyer, Journal of The Electrochemical Society, 2016, 163, A1805-A1811.
- [2] A. Kvasha, E. Azaceta, O. Leonet, M. Bengoechea, I. Boyano, R. T. Zaera, I. Meatza, O. Miguel, H.J. Grande, J. A. Blazquez, Electrochimica Acta, 2015, 180, 16–21
- [3] X. Li, A. Dhanabalan, K. Bechtold, C. Wang, Electrochemistry Communications, 2010, 12, 1222–1225.
- [4] H. Liu, G. Wang, J. Liu, S. Qiao, H. Ahn, J. Mater. Chem., 2011, 21, 3046-3052
- [5] X.H. Huang, J.P. Tu, B. Zhang, C.Q. Zhang, Y. Li, Y.F. Yuan, H.M. Wu, Journal of Power Sources, 2006, 20, 541-544
- [6] Y. Zou, Y. Wang, Nanoscale, 2011, 3, 2615-2620
- [7] J. Y. Liu , N. Li , M. D. Goodman , H. G. Zhang , E. S. Epstein , B. Huang , Z. Pan , J. Kim , J. H. Choi , X. J. Huang , J. H. Liu , K. J. Hsia , S. J. Dillon , P. V. Braun , ACS Nano 2015, 9, 1985
- [8] L. M. Sun , X. H. Wang , R. A. Susantyoko , Q. Zhang , J. Mater. Chem. A 2014, 2, 15294
- [9] H. J. Lin , W. Weng , J. Ren , L. B. Qiu , Z. T. Zhang , P. N. Chen , X. L. Chen , J. Deng , Y. G. Wang , H. S. Peng , Adv. Mater. 2014, 26, 1217
- [10] H. Wu , N. Du , H. Zhang , D. R. Yang , J. Mater. Chem. A 2014, 2, 20510
- [11] H. Wu , G. Chan , J. W. Choi , I. Ryu , Y. Yao , M. T. McDowell , S. W. Lee , A. Jackson , Y. Yang , L. B. Hu , Y. Cui , Nat. Nanotechnol. 2012, 7, 310
- [12] F. F. Cao , J. W. Deng , S. Xin , H. X. Ji , O. G. Schmidt , L. J. Wan , Y. G. Guo , Adv. Mater. 2011, 23, 4415
- [13] Y. Fan , Q. Zhang , C. X. Lu , Q. Z. Xiao , X. H. Wang , B. K. Tay , Nanoscale 2013, 5, 1503
- [14] J. Z. Wang , N. Du , H. Zhang , J. X. Yu , D. R. Yang , J. Power Sources 2012, 208, 434
- [15] H. Guan , X. Q. Wang , S. Chen , Y. Bando , D. Golberg , Chem. Commun. 2011, 47, 12098
- [16] L. F. Cui , R. Ruffo , C. K. Chan , H. L. Peng , Y. Cui , Nano Lett. 2008, 9, 491
- [17] C. Lu, Y. Fan, H. Li, Y. Yang, B. K. Tay, E. Teo, Q. Zhang. Carbon. 2013, 63, 54 – 60.

- [18] L. F. Cui , Y. Yang , C. M. Hsu , Y. Cui , Nano Lett. 2009, 9, 3370
- [19] H. Song , H. X. Wang , Z. Lin , X. Jiang , L. Yu , J. Xu , Z. Yu , X. Zhang , Y. Liu , P. He , L. Pan , Y. Shi , H. Zhou, K. Chen. Adv. Funct. Mater. 2016, 26, 524–531
- [20] T. Song, H. Cheng, H. Choi, J. H. Lee, H. Han, D. H. Lee, D. Su Yoo, M. S. Kwon, J. M. Choi, S. G. Doo, H. Chang, J. Xiao, Y. Huang, W. Park, Y. C. Chung, H. Kim, J. A. Rogers, U. Paik. ACS Nano 2012, 6, 303–309.
- [21] T. Song , H. Cheng , K. Town , H. Park , R. W. Black , S. Lee , W. Park , Y. Huang , J. A. Rogers , L. Nazar , U. Paik. Adv. Funct. Mater. 2014, 24, 1458–1464
- [22] H. Kim, Y. Son, C. Park, M. J. Lee, M. Hong, J. Kim, M. Lee, J. Cho, H. C. Choi. Nano Lett. 2015, 15, 4135–4142
- [23] T. Kennedy, M. Bezuidenhout, K. Palaniappan, K. Stokes, M. Brandon, K. M. Ryan. ACS Nano 2015, 9, 7456–7465.
- [24] G. Kim, S. Jeong, J. H. Shin, J. Cho, H. Lee. ACS Nano 2014, 8, 1907-1912.
- [25] J. Wang, Y. He, F. Fan, X. Liu, S. Xia, Y. Liu, C. Harris, H. Li, J. Huang, S.X. Mao, T. Zhu, Nano Letters, 2013, 709-715.